Geophysical Journal International

Geophys. J. Int. (2016) **207,** 1122–1136
Advance Access publication 2016 August 30
GJI Seismology

doi: 10.1093/gji/ggw324

Morphology of seismically slow lower-mantle structures

Sanne Cottaar[1] and Vedran Lekic[2]

[1]*Department of Earth Sciences, University of Cambridge, Cambridge CB3 OEZ, United Kingdom. E-mail: sc845@cam.ac.uk*
[2]*Department of Geology, University of Maryland, College Park, MD 20742, USA*

Accepted 2016 August 25. Received 2016 August 25; in original form 2016 April 12

SUMMARY

Large low shear velocity provinces (LLSVPs), whose origin and dynamic implication remain enigmatic, dominate the lowermost mantle. For decades, seismologists have created increasingly detailed pictures of the LLSVPs through tomographic models constructed with different modeling methodologies, data sets, parametrizations and regularizations. Here, we extend the cluster analysis methodology of Lekic *et al.*, to classify seismic mantle structure in five recent global shear wave speed (V_S) tomographic models into three groups. By restricting the analysis to moving depth windows of the radial profiles of V_S, we assess the vertical extent of features. We also show that three clusters are better than two (or four) when representing the entire lower mantle, as the boundaries of the three clusters more closely follow regions of high lateral V_S gradients. Qualitatively, we relate the anomalously slow cluster to the LLSVPs, the anomalously fast cluster to slab material entering the lower mantle and the neutral cluster to 'background' lower mantle material. We obtain compatible results by repeating the analysis on recent global *P*-wave speed (V_P) models, although we find less agreement across V_P models. We systematically show that the clustering results, even in detail, agree remarkably well with a wide range of local waveform studies. This suggests that the two LLSVPs consist of multiple internal anomalies with a wide variety of morphologies, including shallowly to steeply sloping, and even overhanging, boundaries. Additionally, there are indications of previously unrecognized meso-scale features, which, like the Perm anomaly, are separated from the two main LLSVPs beneath the Pacific and Africa. The observed wide variety of structure size and morphology offers a challenge to recreate in geodynamic models; potentially, the variety can result from various degrees of mixing of several compositionally distinct components. Finally, we obtain new, much larger estimates of the volume/mass occupied by LLSVPs—8.0 per cent $\pm$0.9 ($\mu \pm 1\sigma$) of whole mantle volume and 9.1 per cent $\pm$1.0 ($\mu \pm 1\sigma$) of whole mantle mass—and discuss implications for associating the LLSVPs with the hidden reservoir enriched in heat producing elements.

Key words: Mantle processes; Composition of the mantle; Seismic tomography.

1 INTRODUCTION

The seismic structure at the base of the mantle is dominated by a pair of large low shear wave velocity (V_S) provinces (LLSVPs; e.g. Garnero & McNamara 2008; Dziewonski *et al.* 2010). LLSVPs are bounded by steep lateral gradients in V_S. This is seen both in global tomographic models (e.g. Burke *et al.* 2008; Lekic *et al.* 2012) and in detailed waveform modeling studies of shear waves reflecting and diffracting at the core–mantle boundary (CMB; e.g. Wen *et al.* 2001; To *et al.* 2005; He *et al.* 2006; Takeuchi *et al.* 2008). Sharp changes across LLSVP boundaries are also seen in seismic anisotropy (Wang & Wen 2007a; Cottaar & Romanowicz 2013; Lynner & Long 2014) and compressional wave speed (Frost & Rost 2014). The LLSVPs are characterized by an anticorrelation between bulk sound and shear wave speeds (Su & Dziewonski 1997; Masters *et al.* 2000; Hernlund & Houser 2008). Modeling of the splitting of Earth's free oscillations has suggested that the LLSVPs may be denser than the surrounding mantle (e.g. Ishii & Tromp 1999; Resovsky & Trampert 2003), though their excess density is likely to be less than 1.5 per cent (Kuo & Romanowicz 2002). Together and individually, these observations have been interpreted to indicate the presence of compositional heterogeneity (e.g. Wen *et al.* 2001; Trampert *et al.* 2004).

The role of LLSVPs in the overall mantle dynamics might be significant: LLSVPs have been modeled to be controlled by subducting slabs (e.g. McNamara & Zhong 2005), while others have argued that they may exert control on the planform of convection in the lower mantle (Dziewonski *et al.* 2010). The LLSVPs appear to play a role in controlling the path of true polar wander (Torsvik *et al.* 2006; Dziewonski *et al.* 2010), as well as the locations of

ultra-low velocity zones, which in geodynamic models appear to be preferentially found along their margins (e.g. McNamara *et al.* 2010). The LLSVPs are associated with restored locations of large igneous provinces (Torsvik *et al.* 2006), major hotspots (Burke *et al.* 2008) and Phanerozoic kimberlites (Torsvik *et al.* 2010), although no statistical inference can be made about these features correlating specifically to the interior or the margin of LLSVPs (Austermann *et al.* 2014; Davies *et al.* 2015). These correlations imply that the LLSVPs are long-lived features, which have persisted in the same approximate locations for at least 360 Myr. Dziewonski *et al.* (2010) also argued that LLSVPs were long-lived features based on the fact that they are characterized by a recumbent spherical harmonic degree 2, which is a probabilistically highly unlikely pattern. Additionally, temperature anomalies associated with the LLSVPs create heterogeneity in the CMB heat flux and through that process influence the geodynamo (Olson *et al.* 2010; Zhang & Zhong 2011; Tarduno *et al.* 2015).

A number of hypotheses have been advanced to address the origin of the LLSVPs, including that they represent: accumulation of subducted oceanic crust (e.g. Christensen & Hofmann 1994), primordial thermochemical piles formed by segregation of dense melts (e.g. Lee *et al.* 2010), a residue of basal magma crystallization (Labrosse *et al.* 2007), or a combination of these processes (e.g. Li *et al.* 2014a). The different scenarios likely relate to different morphologies of the LLSVPs. Geodynamic models show different morphologies of LLSVPs depending on the intrinsic density difference with surrounding material and the choice in combinations of temperature-, depth-, or composition-dependent rheology. Typical scenarios are broad stable piles with low-angle slopes and plumes coming off of ridges (e.g. Bull *et al.* 2009; Zhang *et al.* 2010; Li *et al.* 2014a,b) or metastable piles with steep sides and a buoyancy crossover within the pile (Tan *et al.* 2005; Samuel & Bercovici 2006; Bower *et al.* 2013).

Some studies suggest LLSVPs have a purely thermal origin and represent clusters of thermal plumes that look like continuous structures when seen through the lens of seismic tomography (Schuberth *et al.* 2009; Davies *et al.* 2012). In this scenario, plumes would originate from the CMB instead of the top of piles. These studies argue that a purely thermal scenario can also cause steep gradients in V_S, and anticorrelation of bulk and shear velocities might be explained by the presence of post-perovskite. Clues to the purely thermal or thermochemical nature of slow V_S anomalies will lie in further constraining the corresponding bulk sound and density anomalies. This study does not answer this question. Instead, we seek to identify structures which are consistent across tomographic models, map out their spatial distribution, and estimate their volume.

A robust estimate of the volume of LLSVPs is needed for a number of reasons. First, it is necessary for evaluating how realistic competing explanations of their origins are, and quantifying implications for the reservoirs of major and trace elements, noble gases and heat-producing elements. Second, it is needed to assess the geodynamic stability of the LLSVPs over geological time, since the timescale of survival and morphology of LLSVPs depends on their volume. Third, in models where LLSVPs are enriched in heat-producing elements, calculations of convective stability of the LLSVPs going back in time depend crucially on their volume, as do predictions of lateral variations in geoneutrino flux that may be detectable in the near future (Šramek *et al.* 2013). Previous estimates of LLSVP volume are obtained by isocontouring V_S in a global composite model, resulting in 14.2×10^9 km^3 (Burke *et al.* 2008) and by waveform modeling, resulting in 4.9×10^9 km^3 for the African LLSVP only (Wang & Wen 2004).

The nature and origin of the LLSVPs are of fundamental importance since each of the proposed scenarios carries different implications for the thermal, chemical and dynamical evolution of the Earth. Here, we study the morphology and volume of the LLSVPs in the lower mantle as suggested by cluster analysis across five recent whole-mantle tomographic models, in order to identify common features. Lekic *et al.* (2012) applied cluster analysis to radial profiles of the entire lower mantle. This led to the discovery of a meso-scale slow feature beneath Perm, Russia, which is separated from the African and Pacific LLSVPs. Here, we extend the cluster analysis by using a sliding window in the radial direction (Section 2). We obtain estimates of 3-D morphology for the LLSVPs and new meso-scale features (Section 3). The use of a number of tomographic models provides a range of suggested LLSVP volumes, which are all significantly larger than previously proposed. We repeat the analysis on five *P*-wave tomographic models (Section 3.3). We compare the clustering results to local high-resolution waveform studies and discuss the implications of the observed morphology and presence of meso-scale features on global dynamics, and the implications of the observed volume on geochemical inferences (Section 4).

2 METHOD

2.1 Cluster analysis

Cluster analysis is a classical method for identifying and estimating similarities among objects. The method classifies objects into clusters (i.e. groups, families, etc.) whose members are more similar to one another than to members of other clusters (e.g. Romesburg 2004). Classification via cluster analysis is objective in the sense that distance between individual objects, and between groups of objects, is quantified by a distance metric. When the objects are vectors, such as the set of velocities V_k sampled at depths z_k, $k = 1, 2, \ldots, M$, common distance metrics are those based on correlation between the vectors, the $L1$ and $L2$ distance between them, or the cosine of the angle subtended by the vectors in M-dimensional space. In addition to the choice of the distance metric, the number of clusters (N) needs to be specified. Here, we apply k-means cluster analysis with an $L2$ distance metric where the number of clusters is fixed from the start, and we explore the choice of N in Section 2.2.

When applied to profiles of V_S in the uppermost mantle, k-means clustering using either an $L1$ or $L2$ norm distance metric can map out the geographic extents of major tectonic settings, without the introduction of prior information from geological observations made at the surface (Lekic & Romanowicz 2011). When applied to profiles of the entire lower mantle, k-means clustering of five recent tomographic models (Mégnin & Romanowicz 2000; Houser *et al.* 2008; Kustowski *et al.* 2008; Simmons *et al.* 2010; Ritsema *et al.* 2011) retrieves the geographic extents of the LLSVPs, as well as the LLSVP-like, but geographically isolated meso-scale structure called the Perm anomaly (Lekic *et al.* 2012).

In previous work, Lekic *et al.* (2012) applied cluster analysis on the whole lower-mantle V_S profiles, and showed that the resulting geographic distribution of clusters was dominated by structure near the CMB. In contrast, in this study, we seek to map how the geographic extent of the LLSVPs varies with height above the CMB; therefore, we apply k-means cluster analysis of all V_S profiles in

restricted depth ranges using a sliding window. First, we remove and normalize by the mean velocity profiles within each model. Second, we filter the models to exclude power at spherical harmonic degrees >18, because there is lack of intermodel consistency at those short length scales and very little power in the tomographic models. Then, we sample the models at 2562 equally spaced points that are approximately 2° from each other. At each point, the profile of V_S in the depth range $[z_0 - \frac{1}{2}\Delta z, z_0 + \frac{1}{2}\Delta z]$ discretized in 50 km increments is extracted into a vector V_k. z_0 ranges from 800 to 2700 km. We consider a range of Δz values from 100 to 500 km, but focus our discussion on results for $\Delta z = 300$ km. Note that as Δz tends to 0, the advantage of cluster analysis over analysis based on isocontouring diminishes, while larger Δz leads to stronger vertical smearing.

The five global tomographic models used in this study are:

(i) S40RTS (Ritsema *et al.* 2011): Model of variations of isotropic V_S based on Rayleigh wave and overtone dispersion, normal-mode splitting and body wave traveltimes up to spherical harmonic degree 40 and 21 vertical splines.

(ii) Savani (Auer *et al.* 2014): Model of variations of isotropic V_S and radial anisotropy, based on Rayleigh and Love wave fundamental and overtone dispersion and body wave traveltimes. Parametrized with an adaptive grid varying from 1.25° to 5° grid spacing.

(iii) SEMUCBWM1 (French & Romanowicz 2014): Model of variations of isotropic V_S, V_P and radial anisotropy based on full-waveform body, surface waves and normal-mode splitting functions, parametrized with 20 radial cubic b-splines and 10 242 spherical splines.

(iv) SPani (Tesoniero *et al.* 2015): Model for isotropic velocities base on surface waves to the sixth overtone, body waves and mineral physical constraints on the $\frac{\delta \ln V_S}{\delta \ln V_P}$ for a 5° by 5° grid and 28 layers.

(v) ME2016-S (Moulik & Ekström 2016): Model of variations of isotropic V_S and radial anisotropy, based on Rayleigh and Love wave dispersion, normal-mode splitting, body wave traveltimes and full waveforms. Parametrized with 16 radial cubic b-splines and 362 spherical splines.

For comparison, we repeat the cluster analysis for five recent *P*-wave models:

(i) HSML-P (Houser *et al.* 2008): *P*-wave model is jointly inverted with an *S*-wave model, constrained by fundamental mode surface waves and body waves. Parametrization includes 18 layers with 4° by 4° grid.

(ii) GyPSuM (Simmons *et al.* 2010): Joint inversion of *S*- and *P*-wave velocities and density based on body waves, geodynamical observations and mineral physical constraints, parametrized with 275 km grid spacing and 22 layers.

(iii) LLNL_G3Dv3-P (Simmons *et al.* 2012): Purely *P*-wave model based on millions of *P*-wave traveltimes and using 3-D ray tracing. The lower mantle is parametrized by a level 6 tesselation grid and 26 layers.

(iv) SPani (Tesoniero *et al.* 2015): *P*-wave model is jointly inverted with the *S*-wave model used here and similarly parametrized.

(v) ME2016-P (Moulik & Ekström 2016): *P*-wave model is jointly inverted with the *S*-wave model used here and similarly parametrized.

After we cluster all the windowed profiles for each model, we combine the results across different models. Since each tomographic model generally yields a different estimate of the geographic and depth extents of the clusters, we can choose how many models have to agree about the classification of a location for us to be confident in that classification. To assess how well the geographic and depth extents of clusters agree across models, we count up the number of tomographic models that assign a particular location to a particular cluster, and report that 'vote' count as an integer, m.

We have carried out the same analysis on HSML-S (Houser *et al.* 2008), GyPSuM (Simmons *et al.* 2010), TX2011 (Grand 2002) and SP12RTS (Koelemeijer *et al.* 2016), and obtained fairly similar results. However, in order to keep the vote map more easily understandable, we present the results on the five most recent models which are parametrized at least up to degree 18.

2.2 Number of clusters

In seeking to describe the dominant dichotomy of the lowermost mantle—that between the LLSVP and non-LLSVP regions—Lekic *et al.* (2012) set the number of clusters (N) to two. In this study, we relax this assumption and seek to quantitatively determine the N most appropriate for classifying V_S variations in the entire lower mantle. A naive approach might be to prefer N that minimizes the intracluster variance of V_S, but because variance will always decrease with increasing N, this approach is impractical. Instead, we follow a different approach, in which we analyse how well the geographical extents of N clusters agree with regions of elevated lateral gradients of V_S. In other words, if the boundaries of the geographic regions of the clusters identified using a particular choice of distance metric and N correspond to regions in which tomographic models preferentially map out high lateral gradients in V_S, then that choice of N can be considered more appropriate for describing dominant Earth structures.

First, we compute the lateral velocity gradient as the median of the variation in V_S in a 5° spherical cap across the five tomographic models. Then, at each depth, we define high gradient regions as those in which the lateral velocity gradient is more than 2σ greater than the mean gradient at that depth. Finally, we define cluster boundary regions as the locus of locations in which all of the tomographic models agree that a transition from inside ($m = 5$) to outside ($m = 0$) a cluster occurs within a 5° cap. Table 1 shows the fraction of total area and of high velocity region area covered by cluster boundary regions, for three choices of N. As expected, as N increases, so too does the proportion of locations associated with cluster boundaries. As is shown in Table 1, for $N = 2$, the cluster boundaries account for 39.1 per cent of high velocity gradient regions at the base of the mantle (2700 km depth). However, this proportion deteriorates towards shallower depth, where only 6.7 per cent of high gradient regions are represented by cluster boundaries. Introducing an additional cluster, $N = 3$, substantially improves the correlation with high lateral gradients across the entire depth range. Introducing an additional cluster, $N = 4$, further increases the fraction of total area covered by cluster boundaries, but does not significantly improve the agreement between cluster boundaries and high velocity gradient regions.

This analysis shows that the strong gradients in the lowermost mantle can be reasonably represented by two clusters as is done in Lekic *et al.* (2012), but to describe the entire lower-mantle depths, three clusters are needed. This also implies that across the bulk of the lower mantle, both negative and positive anomalies are isolated and surrounded by strong velocity gradients, whereas at the base of the mantle, strong velocity gradients are associated with transitions between negative and positive anomalies.

Applying k-means clustering with $N = 3$ means one cluster is anomalously slow and the other is anomalously fast. From here

Table 1. Fraction of high V_S gradient regions covered by cluster boundaries as a function of number of clusters N. The fraction of total area covered by cluster boundaries, which increases with increasing N, is shown for reference. High V_S gradient regions are defined as those more than 2σ above the mean at each depth.

Region	Two clusters (per cent)	Three clusters (per cent)	Four clusters (per cent)
All locations at 1700 km	2.4	5.2	5.2
High V_S gradients at 1700 km	6.7	25.8	22.2
All locations at 2700 km	4.0	8.3	9.7
High V_S gradients at 2700 km	39.1	64.0	68.4

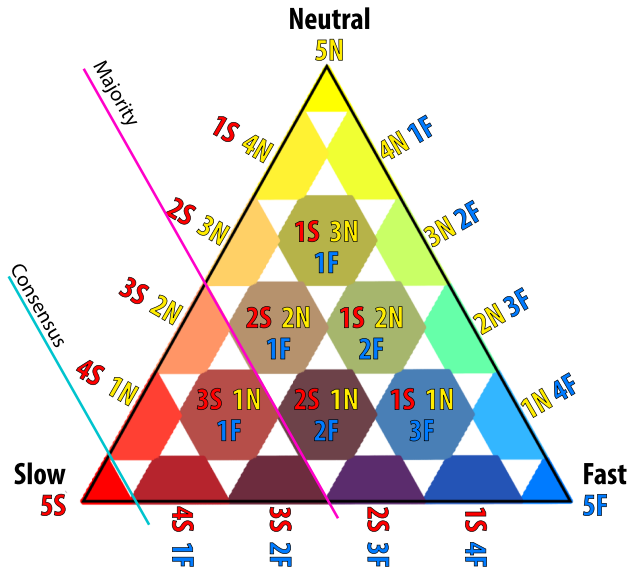

Figure 1. Colour bar used to display the results of the cluster analysis across five tomographic models. The number of votes for each cluster are indicated on or right next to the corresponding colour. The corners of the triangles indicate the colours that represent regions where all tomographic models agree on a single cluster: red for *slow*, yellow for *neutral* and blue for *fast*. The bright colours in the upper edges of the triangle represent regions where disagreement occurs between the *slow* and *neutral* clusters (orangish colours) on the left side, and the *neutral* and *fast* clusters (greenish colours) on the right side. 95.5 per cent of the clustered region is represented by the bright colours in the upper edges. The cases where at least one model votes for *slow* and one for *fast* across models represent 4.5 per cent of the clustered regions, and regions with at least two votes for *slow* and one for *fast* cover less than 0.1 per cent.

on we will refer to the three clusters with relatively fast, neutral and slow shear velocities as *fast*, *neutral* and *slow*, respectively. For effective visualization, we tally the number of tomographic models (m) that assign each location to a particular cluster and translate the ratios of these votes to a red–yellow–blue (ryb) colour scale with red relating to *slow*, yellow to *neutral*, and blue to *fast* (Fig. 1). Regions where the 'vote' is spread across *slow* and *neutral* are coloured in orange colours, while those where it is spread across *fast* and *neutral* are coloured greenish. Regions that are classified as *slow* in some tomographic models and *fast* in others are represented by less saturated and darker colours. In roughly 4.5 per cent of the locations, classification based on one tomographic model be 'opposite' from the others. The extreme case where at least two models classify a location as *fast* and two models classifies it as *slow* (represented by the dark purple colours) is exceedingly rare, occurring in fewer than 0.1 per cent of locations.

3 RESULTS

The vote maps for five depth slices are shown in Fig. 2 centred around the Pacific Ocean and Africa. In the lowermost slice, there is generally good agreement among tomographic models. Analysis with $N = 3$ clusters at this depth results in a similar dichotomy of *fast* and *slow* regions as obtained for $N = 2$ clusters and whole lower-mantle V_S profiles (Lekic *et al.* 2012); the boundaries between the *fast* and *slow* are sharp, and little area is identified as *neutral*.

With increasing height above the CMB, the character of the structures changes and the *neutral* cluster increases in volume. At mid-mantle depths, the *fast* cluster appears as elongated features, mainly in a ring around the Pacific and beneath central Asia. The spatial distribution of the *fast* cluster relates straightforwardly and favourably to cold, downgoing slabs from models of past subduction (e.g. Lithgow-Bertelloni & Richards 1998). The *slow* cluster undergoes an equally dramatic reorganization with height above the CMB, appearing to become more spatially compact. It extends particularly high beneath the Pacific Superswell region, East Africa and Canary and Cape Verde region. Interestingly, some models suggest the *slow* cluster also extends towards the upper mantle beneath Hawaii, Iceland, Jan Mayen, Galapagos, Caroline, Juan Fernandez. However, these features do not tend to be continuous across the entire lower mantle nor to be consistently present across models. Therefore, these plume-like structures might lie just beyond the resolution afforded by our analysis of tomographic models low-pass filtered at spherical harmonic degree 18.

The 3-D extent of the majority vote ($m = 3$) and consensus vote ($m = 5$) for the slow cluster are shown in Fig. 3 (see also Supporting Information). The proportion of total mantle volume and mass occupied by the *fast* and *slow* clusters for different tomographic models and vote (m) thresholds is shown in Table 2; the remainder of the volume/mass is accounted for by the *neutral* cluster. We separate the *slow* cluster into its two primary components—the African and Pacific LLSVPs—and report volumes separately for each. The volume of regions classified as the *slow* cluster is, on average, 8.0 ± 0.9 per cent, and ranges from 7.1 to 9.4 per cent (see Table 2). Similar LLSVP volumes are obtained from the vote maps, with a majority vote ($m > 3$) definition for LLSVP resulting in a total volume of 6.7 per cent. Unsurprisingly, requiring consensus across all models before associating a location with the LLSVP results in a substantially smaller volume estimate of 3.3 per cent. All models except for S40RTS find the African LLSVP to have larger volume than the Pacific LLSVP; the average volume estimate for the African anomaly is ∼30 per cent larger than that of the Pacific LLSVP. Volume of regions classified into the *fast* cluster varies less across models, with an average of 18.2 ± 0.9 per cent, and ranging from 17.0 to 19.2 per cent.

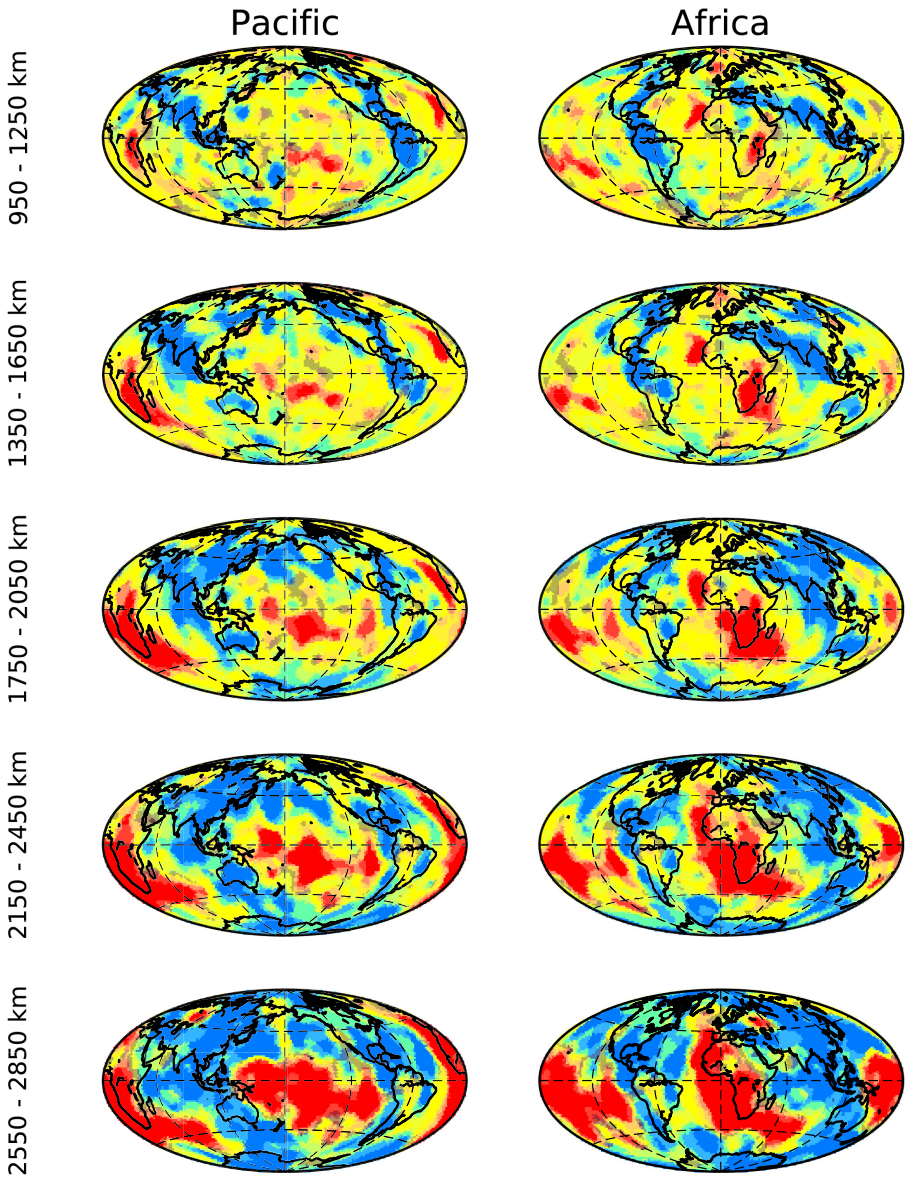

Figure 2. Vote maps obtained by *k-means* cluster analysis of tomographic models, S40RTS, SAVANI, SEMUCB-WM1, SPani and ME2016-S, centred around Pacific Ocean on the left and Africa on the right. The maps in each row correspond to z_0 depths of 1100, 1500, 1900, 2300 and 2700 km. The colour scale is shown in Fig. 1.

3.1 Morphology of LLSVPs or *slow* cluster

Cross-sections through the vote maps show wide variety in LLSVP morphology and suggest the presence of a number of subpiles within the larger piles. We stress that the uniformity of vote maps should only be interpreted as consistency in classification across models and by no means represents uniformity of structure within each cluster domain (see also Supporting Information).

The Pacific LLSVP (Fig. 4) can be roughly divided into three anomalies. The 'West Pacific anomaly' lies beneath the Caroline hotspot to the northeast of Australia. At its centre, it extends 1000 km above the CMB, and is flanked to the west by a flat, ∼300 km high anomaly (Fig. 4cC). To the east, a corridor of a relatively low vertical extent (∼400 km) connects this anomaly to a second anomaly beneath the central Pacific, the 'Superswell anomaly' (Figs 4cC and dD). The Superswell anomaly is more cone-shaped with relatively shallowly sloped sides; its base is thousands of kilometres across and rapidly narrows with height above CMB. This anomaly extends throughout the depth of the lower mantle, and reaches the mantle transition zone beneath the South Pacific Superswell where the Samoan, Marquesas, Tahiti, Pitcairn, Macdonald and Easter hotspots lie. Further to the east, and connected by a vertically thin zone, we find a third anomaly, the 'East Pacific anomaly' (Fig. 4cC). The East Pacific anomaly appears ridge-like, and features particularly steep sides. It extends less than 1000 km high above the CMB, and lies just to the west of the Galagapos and Juan Fernandez hotspots.

The African LLSVP appears as a larger and more continuous feature (Fig. 5). The main anomaly lies beneath southern Africa, but tilts towards the northeast and seems to continue towards the mantle transition zone beneath eastern Africa and Afar, and is therefore named the 'East African anomaly'. The tilting of the anomaly creates an overhang on the northeastern flank

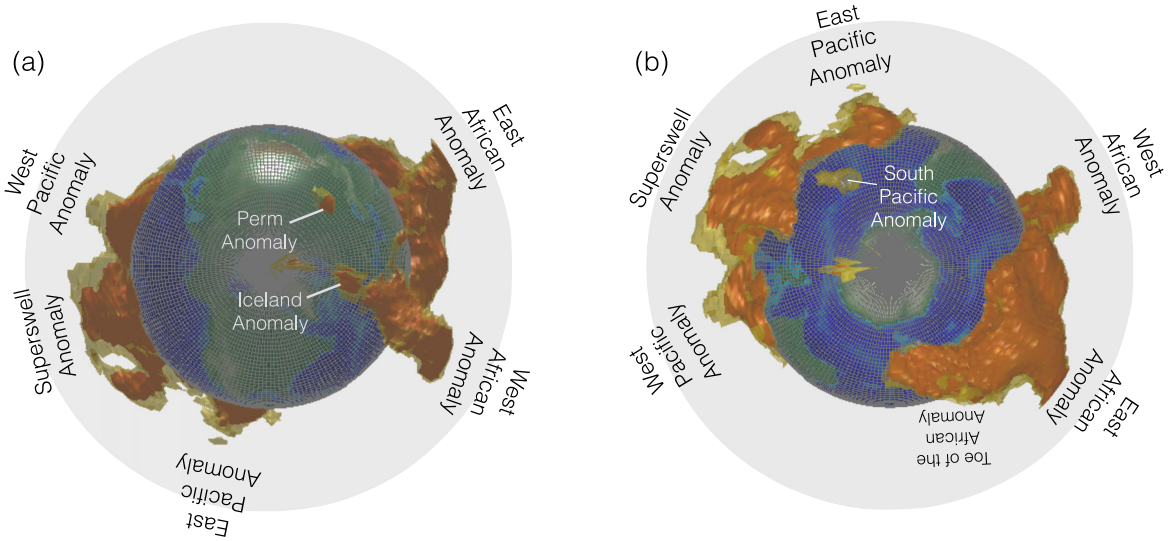

Figure 3. Contour of the votes for the slow cluster for majority ($m = 3$, transparent yellow) and for consensus ($m = 5$, red): the anomalies viewed (a) from the North pole and (b) from the South pole. These plots emphasize the larger size of the African anomalies compared to the Pacific anomalies. Surface topography is projected onto the CMB for reference. See also the Supporting Information.

Table 2. Volume/mass percentages of the mantle of the *slow* and *fast* clusters for different tomographic models and vote (m) thresholds up to 1000 km depth. Reference mantle volume is 8.94×10^{11} km^3 and mantle mass is 4.00×10^{24} kg.

Volume/mass (per cent of the mantle)	*slow* cluster	Pacific *slow*	African *slow*	*fast* cluster
Consensus ($m = 5$)	3.3/3.9	1.2/1.4	2.1/2.5	6.8/7.8
Majority ($m \geq 3$)	6.7/7.7	2.9/3.3	3.9/4.4	17.1/19.5
Average	8.0/9.1	3.5/4.0	4.5/5.1	18.2/20.6
Standard deviation	0.9/1.0	0.9/1.0	0.4/0.4	0.9/1.0
S40RTS	8.6/9.8	4.5/5.1	4.1/4.7	18.4/20.9
SAVANI	7.7/8.8	3.2/3.7	4.5/5.1	17.0/19.3
SEMUCBWM1	9.4/10.7	4.5/5.2	4.8/5.5	17.3/19.6
SPani	7.1/8.2	3.1/3.6	4.0/4.6	19.2/21.8
ME2016-S	7.1/ 8.8	2.1/3.7	5.0/5.1	19.1/19.3

(Fig. 5dD). The same anomaly extends further beneath the Indian Ocean where it tapers out with a shallow slope, which we dub the 'toe of the African anomaly' (Fig. 5cC). The anomaly also extends to the west, where it appears piled up over 1200 km high beneath the Atlantic Ocean. Towards the northwest, a vertically thinner corridor connects this anomaly to the 'West African anomaly'. This anomaly extends across the entire lower mantle beneath the Canary and Cape Verde hotspots. The West African anomaly has steep sides and is less than 2000 km across at its base. The vote map suggest the LLSVP does not extend to beneath Iceland on the CMB, but some models have a separate anomaly beneath Iceland, or a connection of the West Africa anomaly towards Iceland hotspot (Fig. 5bB).

3.2 Meso-scale features

Outside the African and Pacific LLSVPs, the cluster analysis suggests a number of features whose spatial extents are intermediate between that of LLSVPs and ultra-low velocity zones (ULVZ; e.g. McNamara *et al.* 2010). The most apparent meso-scale feature remains the Perm anomaly (Figs 6aA and bB), whose radial extent can be estimated from our analysis to be 400–600 km above the CMB, consistent with previous results from waveform modeling (Lekic *et al.* 2012).

We identify a new meso-scale structure, which we dub the 'South Pacific anomaly', just south of the Pacific LLSVP (Figs 6cC and dD). The consensus vote suggests this anomaly is roughly 10° wide and 400–700 km high, which is similar to the Perm anomaly. A number of the models suggest the anomaly extends hundreds of kilometres higher towards the west, where it might feed into the Louisville hotspot. All models agree, however, that the South Pacific anomaly is an independent feature, which is not connected to the Superswell anomaly.

There are additional regions beneath Iceland (Fig. 5bB) and Kamchatka (Figs 6eE and fF) that might represent meso-scale features, as has been suggested by He *et al.* (2015) and He *et al.* (2014), respectively. However, in these locations, consensus in classification among tomographic models is lacking for an Iceland anomaly and non-existent for a Kamchatka anomaly. We cannot rule out the presence of other Perm-type anomalies—particularly in regions dominated by the *neutral* cluster—whose signature might be masked by regularization or data coverage in the tomographic inversions, or which might be smaller than the resolution of this study (up to degree 18).

3.3 Clustering analysis on *P*-wave models

Vote maps for the clustering analysis across five *P*-wave models are shown in Fig. 7. Qualitatively, they are consistent with those corresponding to *S*-wave models, but show more disagreement among the *P*-wave models. The disagreement is especially notable beneath

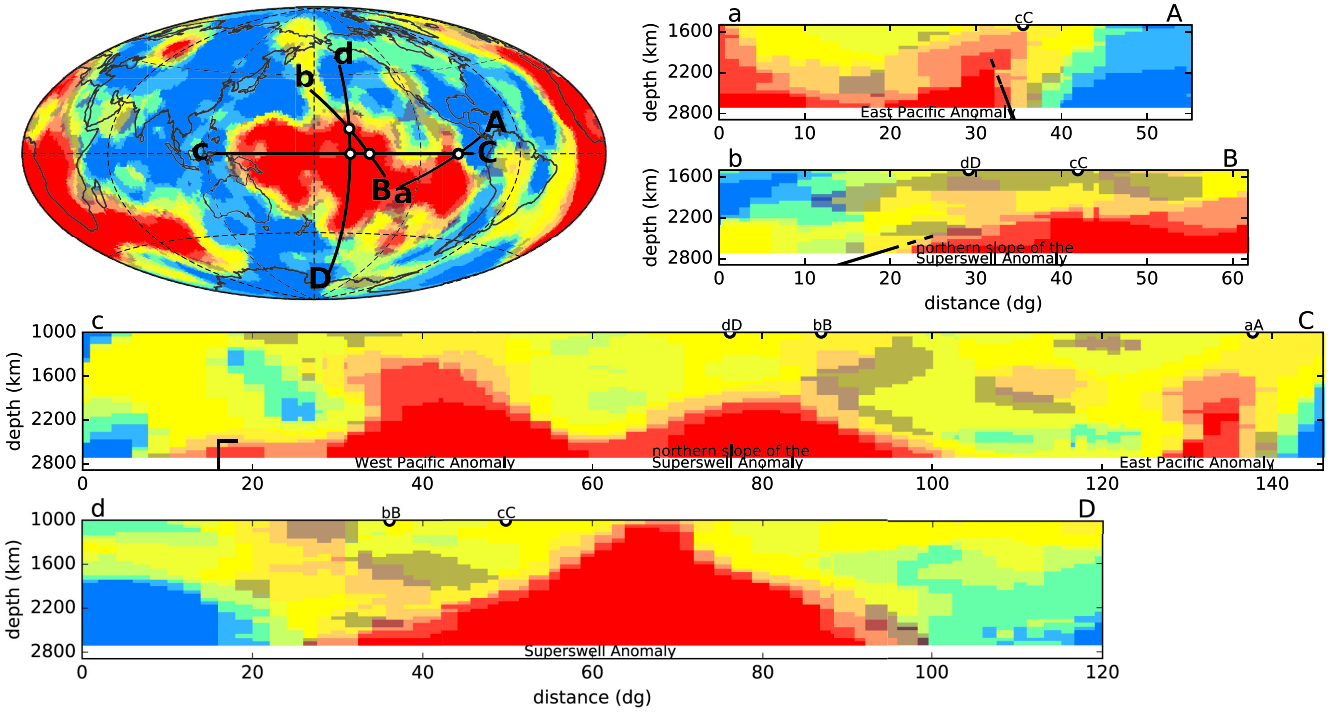

Figure 4. Cross-sections across the Pacific LLSVP showing the vote results for V_S models. Map view shows clustering results at a depth of 2700 km. Cross-sections (aA) and (bB) can be directly compared to those in fig. 7 of Frost & Rost (2014) and the solid black lines represent the boundary as constrained by their *P*-wave data set, while the dashed lines are extrapolated to shallower depths. Cross-section (cC) runs west to east across the LLSVP, illustrating the West Pacific anomaly, the Superswell anomaly and the East Pacific anomaly. Black lines represent the boundaries as modeled by Takeuchi *et al.* (2008). Cross-section (dD) runs north–south across the Superswell anomaly. The colour scale is shown in Fig. 1.

the Southern Pacific, where data coverage is relatively poor in all the models. For the *P*-wave vote maps, 15.4 per cent of areas have disagreement between *fast* and *slow* (compared to only 4.5 per cent for *S*-wave vote map), while 1.2 per cent of areas have at least two votes for both *fast* and *slow* (compared to only 0.1 per cent for *S*-wave vote map).

While there is generally good agreement on the lateral extent of the LLSVPs at the CMB between the slow clusters for *S* and *P* models, there is less agreement on the vertical extent of the various anomalies (see also cross-sections in Figs S1–S3 in the Supporting Information). For example, the Perm anomaly is equally clear in both the *P*- and *S*-wave vote maps, but extends higher in the *P*-wave vote map.

The South Pacific and Icelandic anomalies exhibit less consensus in the *P*-wave vote maps. Surprisingly, the Kamchatka anomaly, which does not appear in the *S*-wave vote maps, is clearly delineated in the *P*-wave model vote map. This difference is particularly striking because data coverage in this area is good for both *P* and *S* waves (due to frequent earthquakes in East Asia and dense receiver coverage in North America), and may represent a new type of lowermost mantle anomaly that is characterized by a bulk modulus reduction accompanied by a less-pronounced weakening of the shear modulus.

4 DISCUSSION

4.1 Comparison with regional seismic studies

Regional studies are complementary to seismic tomography and use traveltime and waveform analysis to constrain the LLSVP structure and amplitudes locally or along a cross-section. These studies tend to use higher frequency body waves compared to global tomography and can map the boundaries of LLSVPs in more detail. In ideal instances, the higher frequency waveforms show complexities that suggest the LLSVP boundaries are sharper than can be captured by tomography. Unfortunately, such studies are constrained to specific favourable geometries, dictated by earthquake and station arrangements appropriate for suitable seismic phases, and by the orientation of the LLSVP boundaries. Therefore, detailed mapping of LLSVP boundaries is not possible in many locations and cannot yet yield a global estimate of the volume and morphology of the LLSVPs. Here, we compare the morphology found in the regional studies to the morphology suggested by our cluster analysis of tomographic V_S models.

Frost & Rost (2014) use high-frequency (0.5–1.6 Hz) *P* waves to map the eastern and northern boundaries of the Pacific LLSVP. At the eastern margin, they find a steep slope of 70°, while at the northern edge, they find a more shallowly sloping margin of 26° (see Figs 4aA and bB and Figs S1aA and bB, Supporting Information). In both locations, the boundary slope inferred from our cluster analysis—both for V_S and V_P models—shows remarkable agreement with these inferences. While the high-frequency *P*-wave illumination geometry is capable of constraining these boundaries in the lowermost few hundred kilometres of the mantle, our vote map suggests the boundaries extend further into the mantle, maintaining a fairly constant angle.

The westernmost edge of the Pacific LLSVP is studied by He *et al.* (2006) and Takeuchi *et al.* (2008) using waveform and traveltime analysis of *S* and *ScS* waves. Both studies find the boundary around 140° at the equator (Fig. 4cC), just east of, but consistent with, cross-section cC (Fig. 3) through our vote map. Takeuchi *et al.* (2008)

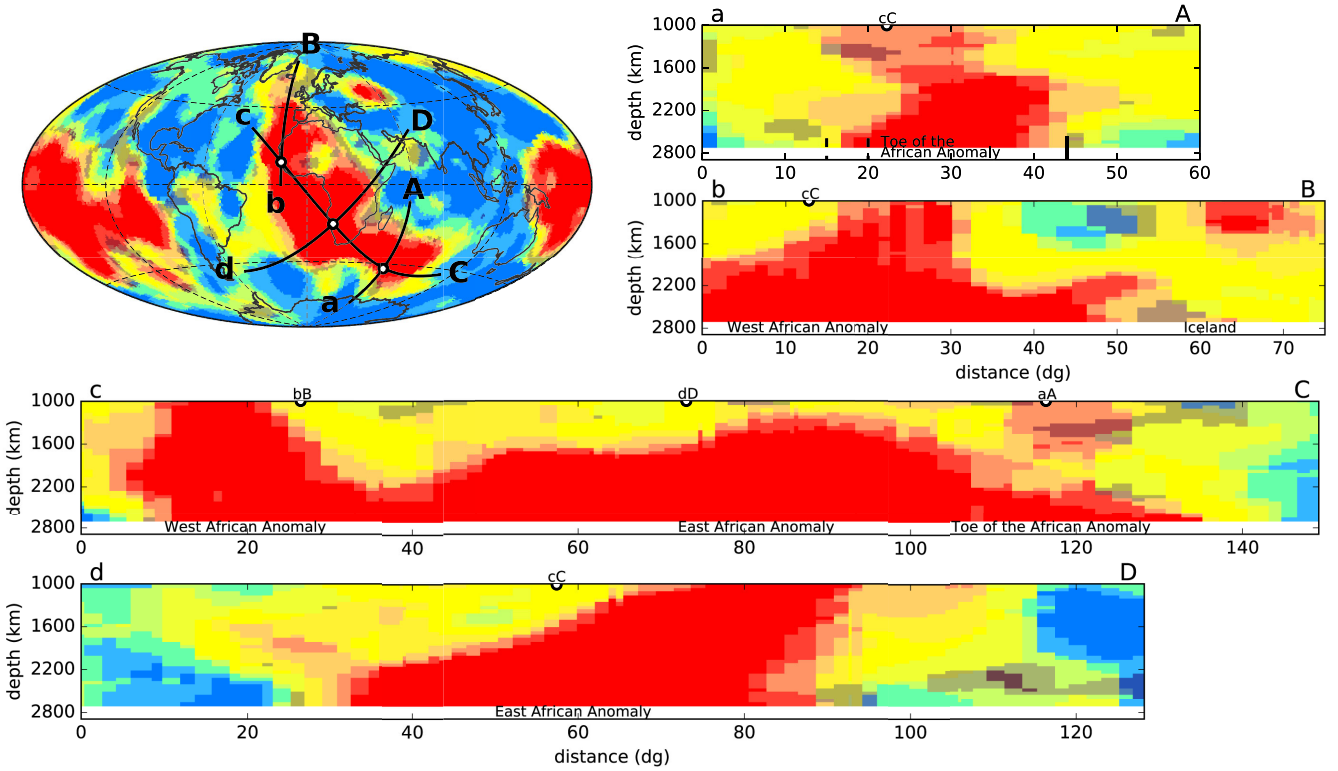

Figure 5. Cross-sections through the African LLSVP showing the vote results for V_S models. Map view shows clustering results at a depth of 2700 km. Cross-section (aA) runs south-to-north across the 'toe' of the African LLSVP. The solid line represents the northern boundary of the LLSVP as modeled by Sun *et al.* (2009), while the two dashed lines bound the approximate region of the studies of Ni *et al.* (2005), To *et al.* (2005), Sun *et al.* (2009) and Cottaar & Romanowicz (2013). Cross-section (bB) runs south-to-north across the West African anomaly to the Iceland anomaly. Cross-section (cC) crosses the length of the anomaly from the West African anomaly across South Africa and beneath the Indian Ocean. Cross-section (dD), running from the southwest to the northeast across eastern Africa, shows the anomalous nature of the East African anomaly: it tilts towards the northeast, creating an overhang. The colour scale is shown in Fig. 1.

report a height for the slow anomaly of 400 km, which agrees well with the results of our study, while He *et al.* (2006) reported a lower height of 220 km. While comparing vertical extents, we should note that the radial sliding window used in the cluster analysis causes potential smearing and vertical uncertainty up to 150 km. Therefore, our results should not be interpreted to favour either study over the other.

Using the waveforms and traveltimes of a suite of shear wave phases sampling the lowermost mantle, He & Wen (2009) infer that the West Pacific anomaly reaches 740 km above the CMB and has steep sides. In He & Wen (2012), they confirm the presence of a separate anomaly to the east, 450 km high and bounded by shallowly sloped sides. These two anomalies are the two westernmost anomalies seen in the vote map in Fig. 4cC. Our results are consistent with the inference of steeper sides of the West Pacific anomaly. Zhao *et al.* (2015) analyse the same anomaly beneath the northern Pacific using observations of waveform broadening and suggest it extends to 600–900 km above the CMB and also argue that it has shallowly sloped sides. The specific geometries used by He & Wen (2012) and Zhao *et al.* (2015) constrain the shallow slopes only on the northern and eastern edge of this anomaly. Our vote map suggests that this anomaly, which we dubbed the Superswell anomaly, does indeed have shallowly sloped sides, but also continues further to the south where it extends throughout the lower mantle (Fig. 4dD). Therefore, the vertical extents inferred by He & Wen (2012) and Zhao *et al.* (2015) would represent apparent heights along the corridor where their data are sensitive to the anomaly, and would not be representative of the maximum height of the anomaly. The height of the Superswell anomaly up to the mantle transition zone beneath the southern Pacific Ocean is independently confirmed by the *P*-wave tomography models of Tanaka *et al.* (2009) and Suetsugu *et al.* (2009).

Multiple investigators have used Sdiff to probe the southern boundary of the African LLSVP beneath the Indian Ocean (Fig. 5aA); they have found both a sharp change in isotropic velocities (Ni *et al.* 2005; To *et al.* 2005; Sun *et al.* 2009) as well as anisotropy (Cottaar & Romanowicz 2013). Our vote map (Fig. 5) shows some disagreement among models on the precise location of this edge, while better agreement suggesting a steep boundary can be seen at the northern edge. The northern boundary appears slightly further south in the vote map than the location proposed by Sun *et al.* (2009).

Sun & Miller (2013) map the LLSVP to the northwest of Africa (Figs 5bB and cC) and find a slow anomaly that extends up to 600 km above the CMB. We find this West African anomaly thins, but extends across the entire lower mantle. The geometry of their data suggests it is sensitive to the region just to the east of the extensive feature seen here, and thus do not capture the maximum height of the anomaly.

One of the most striking comparisons is with the study of Ni *et al.* (2002), which constrains the shape of the African LLSVP along a cross-section from its southwestern to its northeastern edge. Waveform analysis along this corridor suggests a large, slow V_S feature sloping upwards and reaching 1900 km above the CMB (to a depth

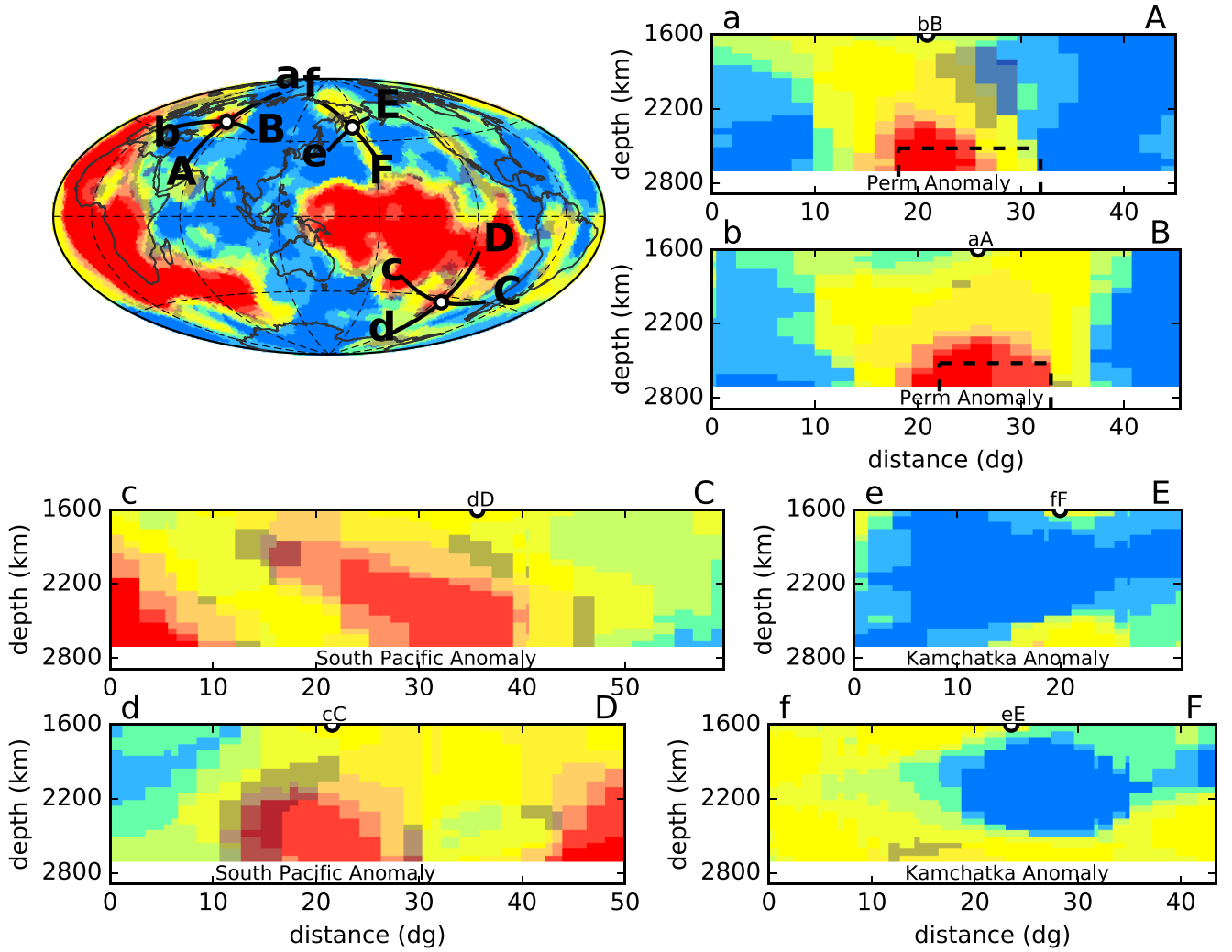

Figure 6. Cross-sections across the various meso-scale features showing the vote results for V_S models. Map view shows clustering results at a depth of 2700 km. Perm anomaly is shown in (aA) and (bB). The black dashed lines show the outline of the cylindrical model proposed in Lekic *et al.* (2012). (cC) and (dD) show the South Pacific anomaly and (eE) and (fF) the Kamchatka anomaly. The colour scale is shown in Fig. 1.

of 1000 km) beneath Eastern Africa. The feature has a characteristic overhang towards the northeast. Wang & Wen (2007b), however, use waveforms along the same cross-section to argue for a very different, 'bell-like' geometry with a height of 1300 km above the CMB. While both studies agree on the southeastern boundary sloping towards the northeast, in the bell-like case of Wang & Wen (2007b), the northeastern boundary slopes towards the southwest, instead of creating an overhang. Our cluster analysis is more consistent with the model of Ni *et al.* (2002), because the vote maps show a northeasterly tilt and overhang along this cross-section (Fig. 5dD). This comparison suggests that classification of structures in tomographic models might provide a means of selecting among multiple possible geometries inferred by studies that forward-model traveltime and waveform features.

Additionally, our vote map suggests the presence of meso-scale features that appear separated from the two main LLSVPs. Lekic *et al.* (2012) used cluster analysis vote maps to identify an isolated anomaly beneath Perm, Russia, and confirmed its presence by modeling delayed Sdiff waveforms from a deep Spain event towards stations in Japan and Taiwan. The data were well fit by a cylindrical model with a V_S reduction of 6 per cent and dimensions outlined in black in Figs 6aA and bB on top of the current vote map. Our vote map suggests that the anomaly may extend a bit higher, up to 400–700 km above the CMB, and that it does not extend as far south as previously modeled. This disagreement is not entirely surprising, since the southern boundary and vertical extent of the Perm anomaly were both poorly constrained by the Sdiff data set used in Lekic *et al.* (2012).

Our results here also suggest a meso-scale anomaly with comparable dimensions to the Perm anomaly to the south of the main Pacific LLSVP. The South Pacific anomaly (Figs 6cC and dD) has not been studied as a separate anomaly in a regional study. However, the S-SKS traveltimes of Ford *et al.* (2006, figs 5a–d) indicate the presence of a slow anomaly in this location with a corridor of relatively faster velocities towards the northwest. Ford *et al.* (2006) do not discuss this aspect of the S-SKS traveltime observations, so future work on independently confirming the existence of the South Pacific anomaly is warranted.

Beneath Iceland, we detect only a slight suggestion of an anomaly that is separated from the African LLSVP (Fig. 5bB). He *et al.* (2015) use ScS-S and sScS-sS traveltimes to argue for a mushroom-shaped anomaly beneath Iceland. The cylindrical stem of the

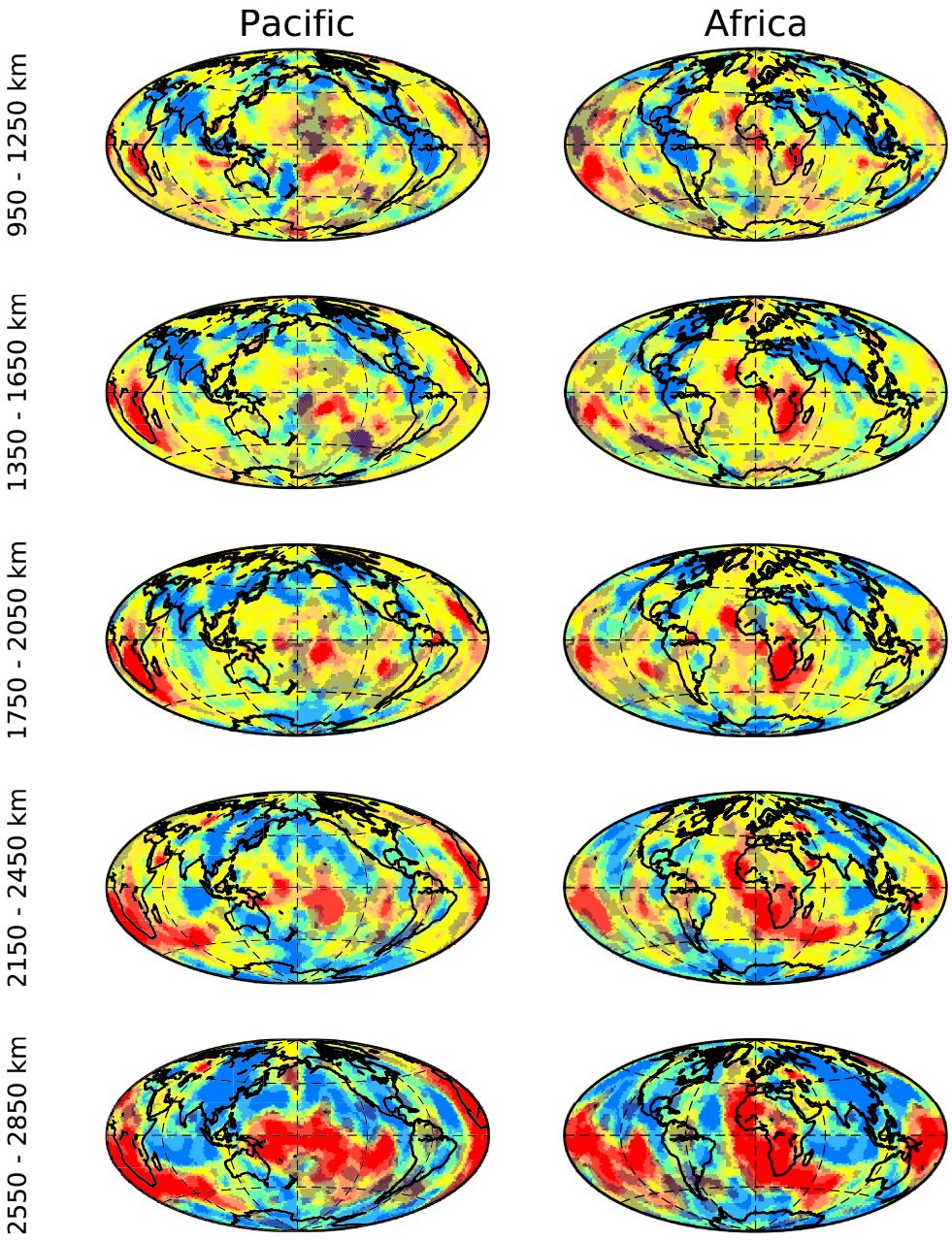

Figure 7. Vote maps obtained by *k-means* cluster analysis of *P*-wave tomographic models, HMSL-P, GyPSuM, LLNL_G3Dv3-P, SPani and ME2016-P, centred around Pacific Ocean on the left and Africa on the right. The maps in each row correspond to z_0 depths of 1100, 1500, 1900, 2300 and 2700 km. The colour scale is shown in Fig. 1.

anomaly is 350 km wide, 250 km high and −6 per cent slow. If this is corrrect, then only the stem appears slow enough in a few tomographic models to be classified with the *slow* cluster in our analysis.

Beneath Kamchatka, He *et al.* (2014) model *S*(diff) phases to infer the presence of an 850 km high anomaly, with a weak −1.2 per cent velocity reduction at the top, increasing in strength to −3 per cent velocity reduction at the bottom. Our cluster analysis vote map for V_S (Figs 6eE and fF) finds only little evidence for a much smaller anomaly in this region. This discrepancy could result from the fact that the amplitudes of the putative Kamchatka anomaly are generally weaker than what is found in waveform studies at LLSVP boundaries and weaker than the −6 per cent velocity anomalies found for the Perm anomaly (Lekic *et al.* 2012) and the Iceland anomaly (He *et al.* 2015). Surprisingly, this anomaly does appear strongly in the vote map for V_P (see Figs S3eE and fF, Supporting Information). This potential lack of V_S reduction and observed discrepancy between the vote maps for V_S and V_P raises the question whether the anomaly beneath Kamchatka has a different composition and origin than the other meso-scale anomalies and the LLSVPs.

Due to their smaller size, meso-scale structures represent more challenging targets to global tomographic imaging; therefore, further regional waveform analysis is needed to confirm or rule out the presence and better characterize the dimensions of meso-scale features detected in this study.

4.2 Geodynamic implications

Our cluster analysis confirms the findings of regional studies that the African and Pacific LLSVPs are made up of smaller anomalies of widely varying vertical extents and with margins that also exhibit a wide range of topographies, from shallowly to steeply sloping. While these anomalies might be connected in the main Pacific and African LLSVPs, there is also a suggestion of at least four separated anomalies (beneath Perm, Iceland, Kamchatka and the South Pacific). The largest 'individual' anomaly by volume is the East African anomaly, which also features an anomalously overhanging wall.

Some geodynamic studies investigating the interaction between subducted slabs and dense piles in the lowermost mantle treat the LLSVPs as two distinct piles or domes and try to reproduce the general round shape of the Pacific LLSVP and elongated shape of the African LLSVP (e.g. Bower *et al.* 2013; Zhong & Rudolph 2015). We analyse the geographic distributions and morphologies of both *slow* and *fast* clusters in order to qualitatively assess to what extent sinking slabs may control the varied morphology of lower-mantle slow structures (e.g. by pushing them around). We find evidence that at least in some locations, steeply sloped margins of the *slow* cluster abut regions with a nearby fast cluster (e.g. the Eastern edge of the Pacific pile in Fig. 4aA). In other locations, however, such as the overhang beneath Eastern Africa (Fig. 5dD), we do not detect nearby fast material and cannot ascribe interaction with slab material to explain the observed morphology. Therefore, while subducting slabs undoubtedly influence the large-scale distribution of LLSVPs material, they do not appear to be the sole determinant of the details of LLSVP boundary morphology. Additionally, the internal morphology of the LLSVPs does not seem to be directly related to subducting slabs. A challenge lies for future geodynamic studies to find scenarios that can generate the variety of internal morphologies described in this study, together with the presence of meso-scale features, even in the absence of direct interaction with subducting slabs.

Geodynamic computations and experiments have investigated the behaviour of an anomalously dense layer at the CMB. Their results range from shallow-sloping piles (e.g. Bull *et al.* 2009) to steep metastable plumes (e.g. Davaille 1999; Simmons *et al.* 2007; Tan *et al.* 2011; Bower *et al.* 2013). Many physical parameters can be varied in such studies, but the most important parameters for the behaviour of a thermochemical pile are its buoyancy and viscosity contrast with the surrounding material (Deschamps & Tackley 2008, 2009). The challenge of explaining the varied behaviours of the individual anomalies might lie in finding a scenario that naturally gives rise to piles with different buoyancy and viscosity contrasts, that is, a scenario in which the piles would vary thermally and/or compositionally.

Wolf *et al.* (2015) explore pile behaviour as a function of Fe content and excess temperature in a purely bridgmanite pile using new thermoelastic constraints. Fe-rich piles lead to stable, passive piles. Only a narrow range of Fe content leads to a metastable pile; the authors give a 4–7 per cent likelihood to such a pile. While differences in Fe enrichment might provide a mechanism to explain different pile morphologies, a question remains as to how piles with varying Fe content are formed in the first place.

Li *et al.* (2014a) explore the mixing of subducted oceanic crust into primordial piles; the mid-ocean-ridge basalt material is episodically flushed into the primordial stable piles and then internally mixed. The authors suggest such a scenario can create both seismic heterogeneity within the piles as well as compositional heterogeneity seen at hotspots with a deep mantle plume. The piles in this scenario remain stable and material is entrained in the mantle plumes. This model suggests a variety in morphology due to an interplay between internal composition and forces from subducting slabs. Qualitatively, this model compares favourably with the results of our analysis as visualized by the vote maps. However, the range of morphologies seen in Li *et al.* (2014a) models does not include a vertically extending and potentially overhanging anomaly as we infer beneath East Africa in our study.

In our vote maps, areas of high consistency of classification across tomographic models are visually represented by uniform colours. This uniformity might give a false impression that the slow anomalies are homogeneous features. Instead, however, an area with constant vote count may represent a wide range of V_S variations within the seismic models (see Figs S4–S6, Supporting Information). This variety in amplitude of V_S variations results from the true internal variation resulting from thermal and compositional variations, but also from the resolution and damping in the tomographic model, which factors will affect the amplitude recovery of an anomaly based on its location and size.

4.3 Comparison and implications of LLSVP volumes

Previous studies have estimated the geometry and volume of the LLSVPs in two ways:

(i) By relating the -1 per cent V_S iso-contour in SMEAN to the edge of the LLSVP and applying a connectivity criterion, Burke *et al.* (2008) mapped the lateral extent of the LLSVPs from the CMB to 1800 km above the CMB, and calculated the volume of the LLSVPs to account for 14.2×10^9 km^3 ($\sim$1.6 per cent of the mantle by volume).

(ii) By systematically mapping the traveltimes and waveforms of phases sampling a wide geographic region, and interpolating in areas that are not properly illuminated by appropriate seismic phases, Wang & Wen (2004) map out the margins of the African LLSVP, and put forth a volume estimate for the African LLSVP of 4.9×10^9 km^3 (or 0.5 per cent of the mantle).

Defining the lateral extent of LLSVPs based on velocity iso-contours is potentially problematic because:

(i) The particular choice of iso-contour level has a substantial effect on estimated volume, and it is unclear how to choose this level objectively.

(ii) The choice of tomographic model in which to perform the calculation is somewhat arbitrary, which is presumably why Burke *et al.* (2008) opt against using a tomographic model, but rather an average of tomographic models for their analysis.

(iii) Iso-contour position is highly sensitive to differences in the fidelity with which amplitudes of lateral velocity variations are retrieved in tomographic models.

On the other hand, defining the extent of LLSVPs based on detailed waveform/traveltime modeling, though in many ways preferable to estimates based on tomography, is fundamentally limited by the geographical distribution of relevant seismic phases at various depths in the lower mantle. Since neither dramatic changes in the global distribution of earthquakes nor instrumentation of ocean basins with seismometers is likely to occur over the coming decades, this geographical limitation is likely to persist into the foreseeable future.

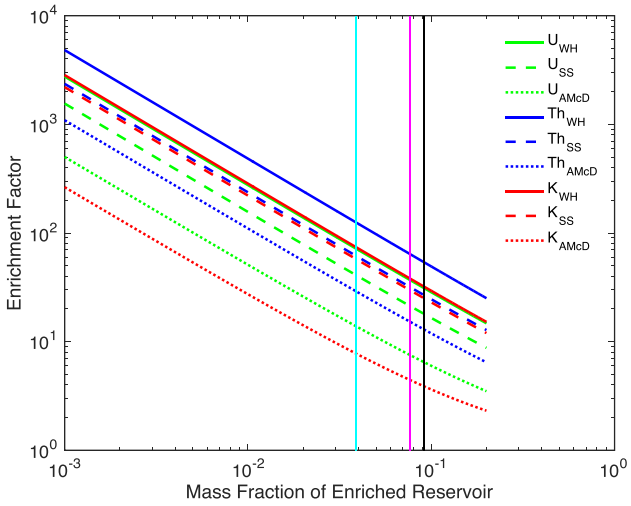

Figure 8. Enrichment factors for the heat producing elements U, Th and K, as a function of mass fraction of the enriched reservoir, computed following Šramek *et al.* (2013). WH—Workman & Hart (2005), SS—Salters & Stracke (2004), AMcD—Arevalo & McDonough (2010).

Cluster analysis with windowed radial V_S profiles offers a way of summarizing the knowledge gained from seismic tomographic models and quantifying the volume of regions classified as seismically *slow*, including the LLSVPs. The remarkable agreement between the geographic extent and morphology inferred from cluster analysis and that imaged by detailed waveform/traveltime studies (see Section 4.1) strongly indicates that volume estimates obtained from cluster analysis are meaningful. In Table 2, we present volume and mass estimates of the *slow* cluster, corresponding to the LLSVPs, for each of the tomographic models, as well as for regions that all models (consensus) or a majority of the models (majority) classify as *slow*. These estimates are several times greater than previously found.

Chemical mass balance arguments can be interpreted to imply the presence of a reservoir of material that is enriched in heat producing elements but is not tapped by mid-ocean ridge basalts (e.g. Hofmann 1997). We follow the approach of Šramek *et al.* (2013) and estimate the enrichment factor of such a lower-mantle enriched reservoir by apportioning a bulk mantle reservoir (obtained by extracting the crust from a bulk silicate Earth model) between a depleted and enriched reservoir. We consider a range of compositions for the depleted reservoir, represented by three recent studies (Salters & Stracke 2004; Workman & Hart 2005; Arevalo & McDonough 2010). We note that this analysis is primarily intended to be illustrative, rather than advocating a particular interpretation of the LLSVP composition. In Fig. 8, we plot the enrichment factor for U, Th and K based on eq. (6) of Šramek *et al.* (2013) as a function of mass fraction of the enriched reservoir. If the bulk of LLSVPs represents this enriched reservoir, then our larger volume estimates for the LLSVPs imply substantially lower enrichment factors than those associated with smaller LLSVP volume estimates. For example, using the Arevalo & McDonough (2010) estimates of the U, Th and K abundances in the depleted mantle, our average LLSVP mass estimate would imply relative enrichment factors of 8.0, 16.4 and 4.7, respectively. The reduced enrichment in heat producing elements will tend to enhance the long-term stability of LLSVP material, allowing for long-term preservation of LLSVPs made up of material with a smaller intrinsic excess density compared to the ambient mantle (e.g. Van Thienen *et al.* 2005).

We stress that our volume estimates represent an upper bound for a hypothetical compositionally distinct pile. This is because the boundaries of the LLSVP cluster do not necessarily represent the boundaries of such a pile; instead, we expect that regions with substantial thermal anomalies surrounding and extending upwards from such a pile would be classified in the *slow* cluster.

5 CONCLUSIONS

We have presented cluster analysis of windowed radial profiles in a number of lower-mantle tomographic models of V_S and V_P to identify robust features across tomographic models and infer the morphology and volume of LLSVPs. We found that classification into three clusters was necessary to obtain good agreement between locations of high V_S horizontal gradients and cluster boundaries. The clustering results across the five different models for each velocity are summarized in vote maps and show good agreement across models for V_S, and correlating features, although with lesser agreement, across models for V_P. The faster-than-average cluster exhibits elongated geographic extents coincident with past subduction, and consistent with the interpretation of this cluster as the seismic signature of descending lithospheric slabs. The slower-than-average cluster exhibits pile-like structures on the CMB related to and characterized by a large variation in morphology. The suggested morphology is in good agreement with previous detailed local waveform studies. The morphology of the vote map suggests an image of the Pacific LLSVP broken up into several smaller anomalies with slopes that vary from shallow (∼30°) to near vertical. The African LLSVP, on the other hand, appears ∼30 per cent larger and includes a flank that overhangs. In addition to the previously imaged Perm anomaly, we identify a new meso-scale feature in the South Pacific, and describe other regions where a smaller slow anomaly might be present.

We hope the cluster analysis we present will both help guide future waveform studies toward regions of interest, and provide an initial model of feature geometry. The vote map can also provide a consensus model to be compared against predictions of geodynamic models testing various compositional and origin scenarios for the LLSVPs. Our proposed LLSVP morphology presents a challenge to our understanding of the deep Earth. This is because it exhibits a wide variation in LLSVP boundary topographies, from shallowly sloped to steeply dipping and even overhanging, as well as multiple meso-scale features not clearly associated with any LLSVP. A central question here is if the diversity in pile behaviour seen can be reproduced by a single composition in combination with interaction with slabs, or if variations in composition in the various anomalies are required. Finally, the reference LLSVP volumes we propose can inform hypotheses concerning the origin of LLSVPs through their geochemical evolution in trace and heat producing elements.

ACKNOWLEDGEMENTS

We thank W.F. McDonough for thoughtful discussion and comments that have contributed to the conceptualization of this work. We thank the editor, Lapo Boschi, and the reviewers, Fabio Cammarano and Andrew Schaeffer, for their suggestions and constructive feedback. VL acknowledges support from the NSF (EAR1352214) and the Packard Foundation. SC is partially funded by the Drapers' Company Research Fellowship from Pembroke College, Cambridge. Part of the research was conducted at CIDER summer programme.

REFERENCES

Arevalo, R. & McDonough, W.F., 2010. Chemical variations and regional diversity observed in MORB, *Chem. Geol.,* **271**(1–2), 70–85.

Auer, L., Boschi, L., Becker, T.W., Nissen-Meyer, T. & Giardini, D., 2014. Savani: a variable resolution whole-mantle model of anisotropic shear velocity variations based on multiple data sets, *J. geophys. Res.,* **119**(4), 3006–3034.

Austermann, J., Kaye, B.T., Mitrovica, J.X. & Huybers, P., 2014. A statistical analysis of the correlation between large igneous provinces and lower mantle seismic structure, *Geophys. J. Int.,* **197**(1), 1–9.

Bower, D.J., Gurnis, M. & Seton, M., 2013. Lower mantle structure from paleogeographically constrained dynamic Earth models, *Geochem. Geophys. Geosyst.,* **14**(1), 44–63.

Bull, A., McNamara, A. & Ritsema, J., 2009. Synthetic tomography of plume clusters and thermochemical piles, *Earth planet. Sci. Lett.,* **278**(3–4), 152–162.

Burke, K., Steinberger, B., Torsvik, T.H. & Smethurst, M.A., 2008. Plume generation zones at the margins of large low shear velocity provinces on the core–mantle boundary, *Earth planet. Sci. Lett.,* **265**(1–2), 49–60.

Christensen, U.R. & Hofmann, A.W., 1994. Segregation of subducted oceanic crust in the convecting mantle, *J. geophys. Res.,* **99**(B10), 19 867–19 884.

Cottaar, S. & Romanowicz, B., 2013. Observations of changing anisotropy across the southern margin of the African LLSVP, *Geophys. J. Int.,* **195**(2), 1184–1195.

Davaille, A., 1999. Simultaneous generation of hotspots and superswells by convection in a heterogeneous planetary mantle, *Nature,* **402,** 756–760.

Davies, D., Goes, S., Davies, J., Shuberth, B., Bunge, H.-P. & Ritsema, J., 2012. Reconciling dynamic and seismic models of Earth's lower mantle: the dominant role of thermal heterogeneity, *Earth planet. Sci. Lett.,* **353,** 253–269.

Davies, D., Goes, S. & Sambridge, M., 2015. On the relationship between volcanic hotspot locations, the reconstructed eruption sites of large igneous provinces and deep mantle seismic structure, *Earth planet. Sci. Lett.,* **411,** 121–130.

Deschamps, F. & Tackley, P.J., 2008. Searching for models of thermo-chemical convection that explain probabilistic tomography, *Phys. Earth planet. Inter.,* **171**(1–4), 357–373.

Deschamps, F. & Tackley, P.J., 2009. Searching for models of thermo-chemical convection that explain probabilistic tomography. IIInfluence of physical and compositional parameters, *Phys. Earth planet. Inter.,* **176**(1–2), 1–18.

Dziewonski, A.M., Lekic, V. & Romanowicz, B.A., 2010. Mantle anchor structure: an argument for bottom up tectonics, *Earth planet. Sci. Lett.,* **299**(1), 69–79.

Ford, S., Garnero, E. & McNamara, A., 2006. A strong lateral shear velocity gradient and anisotropy heterogeneity in the lowermost mantle beneath the southern Pacific, *J. geophys. Res.,* **111**(B3), doi:10.1029/2004JB003574.

French, S.W. & Romanowicz, B.A., 2014. Whole-mantle radially anisotropic shear velocity structure from spectral-element waveform tomography, *Geophys. J. Int.,* **199**(3), 1303–1327.

Frost, D.A. & Rost, S., 2014. The P-wave boundary of the large-low shear velocity province beneath the Pacific, *Earth planet. Sci. Lett.,* **403,** 380–392.

Garnero, E.J. & McNamara, A.K., 2008. Structure and dynamics of Earth's lower mantle, *Science,* **320**(5876), 626–628.

Grand, S., 2002. Mantle shearwave tomography and the fate of subducted slabs, *Phil. Trans. R. Soc. A,* **360**(1800), 2475–2491.

He, Y. & Wen, L., 2009. Structural features and shear-velocity structure of the "Pacific Anomaly", *J. geophys. Res.,* **114,** B02309, doi:10.1029/2008JB005814.

He, Y. & Wen, L., 2012. Geographic boundary of the Pacific Anomaly and its geometry and transitional structure in the north, *J. geophys. Res.,* **117**(B9), doi:10.1029/2012JB009436.

He, Y., Wen, L. & Zheng, T., 2006. Geographic boundary and shear wave velocity structure of the Pacific anomaly near the coremantle boundary beneath western Pacific, *Earth planet. Sci. Lett.,* **244**(1–2), 302–314.

He, Y., Wen, L. & Zheng, T., 2014. Seismic evidence for an 850 km thick low-velocity structure in the Earth's lowermost mantle beneath Kamchatka, *Geophys. Res. Lett.,* **41**(20), 7073–7079.

He, Y., Wen, L., Capdeville, Y. & Zhao, L., 2015. Seismic evidence for an Iceland thermo-chemical plume in the Earth's lowermost mantle, *Earth planet. Sci. Lett.,* **417,** 19–27.

Hernlund, J.W. & Houser, C., 2008. On the statistical distribution of seismic velocities in Earth's deep mantle, *Earth planet. Sci. Lett.,* **265**(3), 423–437.

Hofmann, A.W., 1997. Mantle geochemistry: the message from oceanic volcanism, *Nature,* **385**(6613), 219–229.

Houser, C., Masters, G., Shearer, P. & Laske, G., 2008. Shear and compressional velocity models of the mantle from cluster analysis of long-period waveforms, *Geophys. J. Int.,* **174**(1), 195–212.

Ishii, M. & Tromp, J., 1999. Normal-mode and free-air gravity constraints on lateral variations in velocity and density of Earth's mantle, *Science,* **285,** 1231–1236.

Koelemeijer, P., Ritsema, J., Deuss, A. & van Heijst, H.-J., 2016. SP12RTS: a degree-12 model of shear- and compressional-wave velocity for Earth's mantle, *Geophys. J. Int.,* **204**(2), 1024–1039.

Kuo, C. & Romanowicz, B., 2002. On the resolution of density anomalies in the Earth mantle using spectral fitting of normal mode data, *Geophys. J. Int.,* **150,** 162–179.

Kustowski, B., Ekström, G. & Dziewoński, A.M., 2008. Anisotropic shear-wave velocity structure of the Earth's mantle: a global model, *J. geophys. Res.,* **113,** B06306, doi:10.1029/2007JB005169.

Labrosse, S., Hernlund, J. & Coltice, N., 2007. A crystallizing dense magma ocean at the base of the Earths mantle, *Nature,* **450**(7171), 866–869.

Lee, C.-T.A., Luffi, P., Höink, T., Li, J., Dasgupta, R. & Hernlund, J., 2010. Upside-down differentiation and generation of a primordial lower mantle, *Nature,* **463**(7283), 930–933.

Lekic, V. & Romanowicz, B., 2011. Tectonic regionalization without a priori information: a cluster analysis of upper mantle tomography, *Earth planet. Sci. Lett.,* **308**(1), 151–160.

Lekic, V., Cottaar, S., Dziewonski, A.M. & Romanowicz, B., 2012. Cluster analysis of global lower mantle tomography: a new class of structure and implications for chemical heterogeneity, *Earth planet. Sci. Lett.,* **357–358,** 68–77.

Li, M., McNamara, A.K. & Garnero, E.J., 2014a. Chemical complexity of hotspots caused by cycling oceanic crust through mantle reservoirs, *Nature Geosci.,* **7**(5), 366–370.

Li, Y., Deschamps, F. & Tackley, P.J., 2014b. The stability and structure of primordial reservoirs in the lower mantle: insights from models of thermo-chemical convection in three-dimensional spherical geometry, *Geophys. J. Int.,* **199**(2), 914–930.

Lithgow-Bertelloni, C. & Richards, M.A., 1998. The dynamics of Cenozoic and Mesozoic plate motions, *Rev. Geophys.,* **36**(1), 27–78.

Lynner, C. & Long, M.D., 2014. Lowermost mantle anisotropy and deformation along the boundary of the African llsvp, *Geophys. Res. Lett.,* **41**(10), 3447–3454.

Masters, G., Laske, G., Bolton, H. & Dziewonski, A., 2000. The relative behavior of shear velocity, bulk sound speed, and compressional velocity in the mantle: implications for chemical and thermal structure, *Geophys. Monogr. Ser. Am. Geophys. Un.,* **117,** 63–88.

McNamara, A.K. & Zhong, S., 2005. Thermochemical structures beneath Africa and the Pacific Ocean, *Nature,* **437**(7062), 1136–1139.

McNamara, A.K., Garnero, E.J. & Rost, S., 2010. Tracking deep mantle reservoirs with ultra-low velocity zones, *Earth planet. Sci. Lett.,* **299**(1–2), 1–9.

Mégnin, C. & Romanowicz, B., 2000. The three-dimensional shear velocity structure of the mantle from the inversion of body, surface and higher-mode wave forms, *Geophys. J. Int.,* **143,** 709–728.

Moulik, P. & Ekström, G., 2016. The relationships between large-scale variations in shear velocity, density, and compressional velocity in the Earth's mantle, *J. geophys. Res.,* **121**(4), 2737–2771.

Ni, S., Tan, E., Gurnis, M. & Helmberger, D., 2002. Sharp sides to the African superplume, *Science,* **296**(5574), 1850–1853.

Ni, S. V., Helmberger, D. & Tromp, J., 2005. Three-dimensional structure of the African superplume from waveform modelling, *Geophys. J. Int.,* **161**(2), 283–294.

Olson, P.L., Coe, R.S., Driscoll, P.E., Glatzmaier, G.A. & Roberts, P.H., 2010. Geodynamo reversal frequency and heterogeneous coremantle boundary heat flow, *Phys. Earth planet. Int.,* **180**(1–2), 66–79.

Resovsky, J. & Trampert, J., 2003. Using probabilistic seismic tomography to test mantle velocity-density relationships, *Earth planet. Sci. Lett.,* **215,** 121–134.

Ritsema, J., Deuss, A., van Heijst, H.J. & Woodhouse, J., 2011. S40RTS: a degree-40 shear-velocity model for the mantle from new Rayleigh wave dispersion, teleseismic traveltime and normal-mode splitting function, *Geophys. J. Int.,* **184**(3), 1223–1236.

Romesburg, C., 2004. *Cluster Analysis for Researchers,* Lulu Press.

Salters, V.J.M. & Stracke, A., 2004. Composition of the depleted mantle, *Geochem. Geophys. Geosyst.,* **5**(5), doi:10.1029/2003GC000597.

Samuel, H. & Bercovici, D., 2006. Oscillating and stagnating plumes in the Earth's lower mantle, *Earth planet. Sci. Lett.,* **248**(1–2), 90–105.

Schuberth, B. S.A., Bunge, H.-P., Steinle-Neumann, G., Moder, C. & Oeser, J., 2009. Thermal versus elastic heterogeneity in high-resolution mantle circulation models with pyrolite composition: high plume excess temperatures in the lowermost mantle, *Geochem. Geophys. Geosyst.,* **10**(1), doi:10.1029/2009GC002401.

Simmons, N.A., Forte, A.M. & Grand, S.P., 2007. Thermochemical structure and dynamics of the African superplume, *Geophys. Res. Lett.,* **34**(2), L02301, doi:10.1029/2006GL028009.

Simmons, N.A., Forte, A.M., Boschi, L. & Grand, S.P., 2010. GyPSuM: a joint tomographic model of mantle density and seismic wave speeds, *J. geophys. Res.,* **115**(B12), B12310, doi:10.1029/2010JB007631.

Simmons, N.A., Myers, S.C., Johanneson, G. & Matzel, E., 2012. LLNL-G3Dv3: global P wave tomography model for improved regional and teleseismic travel time prediction, *J. geophys. Res.,* **117**(B10), doi:10.1029/2012JB009525.

Šramek, O., McDonough, W.F., Kite, E.S., Lekic, V., Dye, S.T. & Zhong, S., 2013. Geophysical and geochemical constraints on geoneutrino fluxes from Earths mantle, *Earth planet. Sci. Lett.,* **361,** 356–366.

Su, W.-J. & Dziewonski, A., 1997. Simoultaneous inversions for 3-D variations in shear and bulk velocity in the Mantle, *Phys. Earth planet. Inter.,* **100,** 135–156.

Suetsugu, D. *et al.*, 2009. South Pacific mantle plumes imaged by seismic observation on islands and seafloor, *Geochem. Geophys. Geosyst.,* **10**(11), doi:10.1029/2009GC002533.

Sun, D. & Miller, M.S., 2013. Study of the western edge of the African Large Low Shear Velocity Province, *Geochem. Geophys. Geosyst.,* **14**(8), 3109–3125.

Sun, D., Helmberger, D., Ni, S. & Bower, D., 2009. Direct measures of lateral velocity variation in the deep Earth, *J. geophys. Res.,* **114**(B5), B05303, doi:10.1029/2008JB005873.

Takeuchi, N., Morita, Y., Xuyen, N. & Zung, N., 2008. Extent of the low-velocity region in the lowermost mantle beneath the western Pacific detected by the Vietnamese Broadband Seismograph Array, *Geophys. Res. Lett.,* **35**(5), L05307, doi:10.1029/2008GL033197.

Tan, E., Leng, W., Zhong, A. & Gurnis, M., 2005. Metastable superplumes and mantle compressibility, *Geophys. Res. Lett.,* **32**(20), L20307, doi:10.1029/2005GL024190.

Tan, E., Leng, W. & Zhong, S., 2011. On the location of plumes and lateral movement of thermochemical structures with high bulk modulus in the 3-D compressible mantle, *Geochem. Geophys. Geosyst.,* **12,** Q07005, doi:10.1029/2011GC003665.

Tanaka, S., Suetsugu, D., Shiobara, H., Sugioka, H., Kanazawa, T., Fukao, Y., Barruol, G. & Reymond, D., 2009. On the vertical extent of the large low shear velocity province beneath the South Pacific Superswell, *Geophys. Res. Lett.,* **36**(7), doi:10.1029/2009GL037568.

Tarduno, J.A., Watkeys, M.K., Huffman, T.N., Cottrell, R.D., Blackman, E.G., Wendt, A., Scribner, C.A. & Wagner, C.L., 2015. Antiquity of the South Atlantic Anomaly and evidence for top-down control on the geodynamo, *Nat. Commun.,* **6,** 7865, doi:10.1038/ncomms8865.

Tesoniero, A., Auer, L., Boschi, L. & Cammarano, F., 2015. Hydration of marginal basins and compositional variations within the continental lithospheric mantle inferred from a new global model of shear and compressional velocity, *J. geophys. Res.,* **120**(11), 7789–7813.

To, A., Romanowicz, B., Capdeville, Y. & Takeuchi, N., 2005. 3D effects of sharp boundaries at the borders of the African and Pacific Superplumes: observation and modeling, *Earth planet. Sci. Lett.,* **233**(1–2), 1447–1460.

Torsvik, T.H., Smethurst, M.A., Burke, K. & Steinberger, B., 2006. Large igneous provinces generated from the margins of the large low-velocity provinces in the deep mantle, *Geophys. J. Int.,* **167**(3), 1447–1460.

Torsvik, T.H., Burke, K., Steinberger, B., Webb, S.J. & Ashwal, L.D., 2010. Diamonds sampled by plumes from the core–mantle boundary, *Nature,* **466**(7304), 352–355.

Trampert, J., Deschamps, F., Resovsky, J. & Yuen, D., 2004. Probabilistic tomography maps chemical heterogenities throughout the mantle, *Science,* **306,** 853–856.

Van Thienen, P., Van Summeren, J., Van der Hilst, R., Van den Berg, A. & Vlaar, N., 2005. *Earth's Deep Mantle: Structure, Composition, and Evolution*, Geophysical Monograph Series, Vol. 160, American Geophysical Union, Washington, DC.

Wang, Y. & Wen, L., 2004. Mapping the geometry and geographic distribution of a very low velocity province at the base of the Earth's mantle, *J. geophys. Res.,* **109**(B10), doi:10.1029/2003JB002674.

Wang, Y. & Wen, L., 2007a. Complex seismic anisotropy at the border of a very low velocity province at the base of the Earth's mantle, *J. geophys. Res.,* **112**(B9), 1–11.

Wang, Y. & Wen, L., 2007b. Geometry and *P* and *S* velocity structure of the African Anomaly, *J. geophys. Res.,* **112**(B5), doi:10.1029/2006JB004483.

Wen, L., Silver, P., James, D. & Kuehnel, R., 2001. Seismic evidence for a thermo-chemical boundary at the base of the Earth's mantle, *Earth planet. Sci. Lett.,* **189**(3), 141–153.

Wolf, A.S., Jackson, J.M., Dera, P. & Prakapenka, V.B., 2015. The thermal equation of state of (Mg, Fe)SiO_3 bridgmanite (perovskite) and implications for lower mantle structures, *J. geophys. Res.,* **120**(11), 7460–7489.

Workman, R.K. & Hart, S.R., 2005. Major and trace element composition of the depleted MORB mantle (DMM), *Earth planet. Sci. Lett.,* **231**(1–2), 53–72.

Zhang, N. & Zhong, S., 2011. Heat fluxes at the Earth's surface and core,Äìmantle boundary since Pangea formation and their implications for the geomagnetic superchrons, *Earth planet. Sci. Lett.,* **306**(3–4), 205–216.

Zhang, N., Zhong, S., Leng, W. & Li, Z.-X., 2010. A model for the evolution of the Earth's mantle structure since the Early Paleozoic, *J. geophys. Res.,* **115**(B6), B06401, doi:10.1029/2009JB006896.

Zhao, C., Garnero, E.J., McNamara, A.K., Schmerr, N. & Carlson, R.W., 2015. Seismic evidence for a chemically distinct thermochemical reservoir in Earth's deep mantle beneath Hawaii, *Earth planet. Sci. Lett.,* **426,** 143–153.

Zhong, S. & Rudolph, M.L., 2015. On the temporal evolution of long-wavelength mantle structure of the Earth since the early Paleozoic, *Geochem. Geophys. Geosyst.,* **16**(5), 1599–1615.

SUPPORTING INFORMATION

Additional Supporting Information may be found in the online version of this paper:

Figure S1. Cross-sections across the Pacific LLSVP showing the vote results for V_P models.

Figure S2. Cross-sections through the African LLSVP showing the vote results for V_P models.

Figure S3. Cross-sections across the various meso-scale features showing the vote results for V_P models.

Figure S4. Cross-sections across the Pacific LLSVP showing the mean velocity in V_S models and the contours for $m = 4$ (slow in red, neutral in yellow, and fast in blue).

Figure S5. Cross-sections through the African LLSVP showing the mean velocity in V_S models and the contours for $m = 4$ (slow in red, neutral in yellow, and fast in blue).
Figure S6. Cross-sections across the various meso-scale features showing the mean velocity in V_S models and the contours for $m = 4$ (slow in red, neutral in yellow, and fast in blue).
Figure S7. Additional snapshots of 3-D projection showing the votes for the slow cluster for majority ($m = 3$, transparent yellow) and for consensus ($m = 5$, red) without annotations.

(http://gji.oxfordjournals.org/lookup/suppl/doi:10.1093/gji/ggw324/-/DC1).

Please note: Oxford University Press is not responsible for the content or functionality of any supporting materials supplied by the authors. Any queries (other than missing material) should be directed to the corresponding author for the paper.